RESEARCH ARTICLE

FFT-Based Frequency Detection and Interference Analysis for NLOS MIMO-OCC

SHIVANI RAJENDRA TELI[ID]1, **VICENTE MATUS ICAZA**2, **STANISLAV VÍTEK**[ID]1,
RAFAEL PEREZ-JIMENEZ[ID]2, **ZABIH GHASSEMLOOY**[ID]3, (Senior Member, IEEE),
AND STANISLAV ZVANOVEC[ID]1, (Senior Member, IEEE)

[1]Department of Electromagnetic Field, Faculty of Electrical Engineering, Czech Technical University in Prague, 16627 Prague, Czech Republic
[2]Institute for Technological Development and Innovation in Communications, Universidad de Las Palmas de Gran Canaria, 35001 Las Palmas, Spain
[3]Optical Communications Research Group, Faculty of Engineering and Environment, Northumbria University, NE1 8ST Newcastle-upon-Tyne, U.K.

Corresponding author: Shivani Rajendra Teli (telishiv@fel.cvut.cz)

ABSTRACT In this paper, we provide a solution based on fast Fourier Transform (FFT) for frequency detection and interference analysis in a non-line-of-sight (NLOS) multiple-input multiple-output (MIMO) optical camera communications (OCC) link. The proposed NLOS MIMO-OCC uses two organic light-emitting diodes (OLEDs) and a camera as transmitters (Txs) and the receiver, respectively, and reflections from various surfaces such as plain wall, paper and wooden surfaces. In this paper, for the first time, we analyze the performance of NLOS MIMO-OCC for two indoor scenarios utilizing two OLED Txs that are in phase and modulated at the same modulation frequency f_s and especially when they are out of phase and under different f_s. We carry out FFT for f_s detection and interference analysis for OLEDs operating at different phases and f_s. To analyze the performance of NLOS MIMO-OCC, first FFT-based f_s detection is performed to identify Txs followed by evaluation of the reception success rates R_{rs} for a range of camera exposure times t_{exp} and the gain G_v for a given f_s. The results show that for two OLEDs in phase and different phases at t_{exp} of 1500, G_v of 45 dB and a link span of 2 m, R_{rs} of 94% is achieved at f_s of 600 Hz for the plain wall and paper reflectors. For interference analysis, the proposed FFT analysis gives accurate, i.e., 100 % f_s detection in all the above cases.

INDEX TERMS Organic light emitting diode (OLED), optical camera communications (OCC), non-line-of-sight (NLOS), multiple-input multiple-output (MIMO), fast Fourier transform (FFT), camera, image processing.

I. INTRODUCTION

Researchers have been exploring the use of organic light-emitting diodes (OLEDs) over traditional solid-state lights as transmitters (Txs) in visible light communications (VLC) and optical camera communications (OCC) technologies. A comprehensive optical and electrical characterization, evaluation, simultaneous illumination, and data communication of OLED-based VLC links for indoor applications have been investigated [1], [2]. In our recent publication [3], the

The associate editor coordinating the review of this manuscript and approving it for publication was Yiming Tang[ID].

authors outlined the main advantages of OLEDs including radiation patterns, highly linear power-current characteristics, stable illumination profile, different shapes and sizes as well as their being desirable in camera-based receivers (Rxs) instead of point source detection in complex and dynamic environments. In [4], for the first time, a line-of-sight (LOS) long-range OLED-OCC was proposed for Internet of Things (IoT) applications.

Using OCC technology and a photodetector (PD) array (i.e., a complementary metal-oxide-semiconductor (CMOS) image sensor or a camera)-based Rx, both single-input multiple-output and multiple-input multiple-output (MIMO)

systems can be implemented in indoor environments. Note that the image sensor-based Rx can capture lights from different directions and project them onto different sections of the sensor (i.e., illuminating different parts of the PD array). It is possible to spatially separate incoming light signals using the region of interest (ROI) method and determine their intensities by measuring the pixel value per light source image on the received frame. There are several unique features of OCC, including simultaneous vision and data communications; built-in Rx (i.e., camera) and therefore no need for additional hardware; spatial separation of multiple Txs (i.e., sunlight, street light vehicle lights [5], [6]); improved performance under ambient lighting [7]; and suitable for non-line-of-sight (NLOS) scenarios [8]. In [9], the data rate in MIMO-OCC using an array of red, green and blue (RGB) LEDs was increased by exploiting the advantage of having a two-dimensional space from the captured frames. To deal with the blooming effect in a LOS wavelength division multiplexing (WDM) MIMO-OCC link, a histogram equalization scheme was proposed that helps to adjust image intensities to enhance contrast and, therefore, achieve 100 % data reception rates [10]. Moreover, a two-dimensional convolutional autoencoder was proposed for simultaneous exposure-related intersymbol interference (ISI) equalization and noise mitigation for OCC [11]. The results in [11] showed that the system can mitigate the ISI produced by the exposure time windows with the bit error rates lower than 10^{-5} under optimal signal-to-noise ratio (SNR) conditions.

In dynamic and mobile indoor environments, LOS VLC-OCC links may experience shadowing, blocking, and no availability of LOS paths, limiting link availability, mobility and, ultimately, system performance [12], [14]. To resolve these problems, NLOS VLC-OCC systems can be adopted at the expense of reduced data throughputs, which may not be necessary in low-data rate IoT-based applications [10], [15]. In [3], for the first time, we proposed a single-input multiple-output (SIMO) NLOS-OCC scheme using a curved OLED Tx varying L from 1 to 2 m using non-return-to-zero (NRZ)-OOK modulation format and a ROI and grayscale-based normalization and thresholding algorithm for demodulation. The primary performance analysis was focused on SNR estimation using a binary classification procedure based on a Gaussian mixture model (GMM) to mitigate the attenuation effect due to NLOS links. The NLOS VLC-OCC links, however, still face a few challenges, including *i)* higher losses due to diffuse reflections, which lower the SNR; *ii)* increased levels of interference from other light sources; and *iii)* difficulty in implementation of NLOS MIMO VLC-OCC.

In [16], a DC-biased optical orthogonal frequency division multiplexing (DCO-OFDM) in the NLOS model (i.e., a single-reflection) was investigated to benefit from the enhanced spectral efficiency and easily configurable DC components. Moreover, [17] concluded that a less complex single-fast Fourier transform (FFT)-based Rx is a good candidate for layered asymmetrically clipped OFDM suffering from the LED nonlinearity. In [18], digital signal processing (i.e., a combination of FFT and inverse FFT (IFFT)) was applied to extract the low-frequency part of the 3-70 kHz on-off-keying (OOK) signal at the transmitting side to reduce the impact of LED flicker on human health was proposed. Therefore, FFT and IFFT can be used both for low-frequency baseband and complex modulation formats in LOS and NLOS VLC links to overcome LED nonlinearities as well as to restore the received signal.

According to [19], the reflected optical beams in NLOS VLC-OCC typically have a large illumination footprint, allowing an increased degree of mobility and link tolerance to the user movements. Based on different reflecting materials, such as walls, furniture, and paper decorations, the illumination footprint is expected to vary and affect the NLOS VLC-OCC signal in indoor environments. In this paper, we propose a NLOS MIMO OCC link with two OLEDs and a camera as Txs and the Rx, respectively. The light reflections are from various surfaces, including plain walls, paper, and wooden surfaces, as well as corners of the room. In this paper, for the first time, we evaluate the performance of the proposed NLOS MIMO OCC scheme with two OLED Txs that are *i)* in phase (i.e., synchronized) and transmitting at the same modulation frequency f_s; and *ii)* out of phase and with different f_s. The proposed system is evaluated in terms of the reception success rates R_{rs} for a range of camera exposure times t_{exp} and the gain G_v as well as f_s. FFT is applied for detecting f_s and analyzing interference when both OLEDs transmit at different phase and f_s.

The remaining sections are organized as follows: Section II gives a brief outlook and limitations of the previous related works; Section III provides an overview of the proposed NLOS MIMO OLED-OCC system; Section IV presents experiment results and analysis; Section V summarizes the performance and results of the proposed scheme and Section VI concludes this article along with future outlook.

II. RELATED WORKS
In Table 1, we compare the performance of the proposed NLOS MIMO OLED-OCC link with other NLOS-OCC systems. As previously mentioned, the main motivation for developing this system is to be able to operate in a reflective environment. We, therefore focus mainly on parameters such as the Tx/Rx, modulation format, link span L, and processing algorithm and compare them with other systems.

Note that all the above-listed schemes in Table 1 have focused only on data recovery using various adaptive algorithms. However, different reflective materials and surfaces in indoor environments need to be considered when analyzing NLOS-based systems. Therefore, we propose, for the first time to the best of our knowledge, FFT-based fs detection and interference analysis for NLOS MIMO OLED-OCC used in an indoor environment scenario with different reflective and surface materials.

TABLE 1. Summary of existing NLOS-OCC schemes.

Scheme / System parameter	Tx and Rx	Modulation format	L (m)	Processing algorithm	Interference analysis with varying reflective plain and material
Curved OLED-based NLOS-OCC (SIMO link) [3]	Single UNISAGA OLED; Raspberry Pi camera	NRZ-OOK	2	ROI and grayscale-based normalization and thresholding and GMM for SNR analysis. No FFT	Not analyzed
Long-distance NLOS visible light signal detection [20]	Phosphor-based white-light LED chips; HTC mobile phone	OOK	1.5	Bradley thresholding, 2nd order polynomial thresholding, and quick adaptive thresholding	Not analyzed
Mobile phone camera-based VLC using an NLOS Link [15]	An array of 15 white LEDs; mobile phone camera	NRZ-OOK	1	ROI and grayscale-based normalization and thresholding	Not analyzed
Improved OCC systems using a freeform lens [21]	2 W white LED chip; HUAWEI P30's camera	4-PAM; 8-PAM	0.8	ROI and grayscale-based normalization and thresholding. Complex implementation	Not analyzed
NLOS MIMO space-time division multiplexing using mask matching, equal-gain combining [19] and pilot-aided signal layer estimation [14]	Not specified; Google phone NEXUS 5	OOK	1.3-2.5	Mask matching and pilot-aided signal layer estimation	Not analyzed
NLOS WDM-MIMO OCC with the DBPWR algorithm [22]	RGB Luminus LEDs; Sony IMX60	OOK; multi-level PWM	2	Difference-based pulse width recognition	Not analyzed
Spatial multiplexing for NLOS light-to-camera communications [23]	3 COTS LEDs; iPhone 6s	PSK	1	Superimposed rect-wave division algorithm	Not analyzed
NLOS MIMO space-time division multiplexing visible light OCC [19]	Luxeon rebel LED; Canon Rebel camera	NRZ-OOK	1.3	Mask matching and equal-gain combining	Not analyzed
Proposed NLOS MIMO OLED-OCC	Two UNISAGA OLEDs; Raspberry Pi camera	NRZ-OOK	2	FFT-based f_s detection and interference analysis along with ROI and grayscale-based normalization and thresholding	Yes, performed in various indoor scenarios considering various reflective surfaces

III. NLOS MIMO OLED-BASED OCC

Figure 1 illustrates the proposed NLOS MIMO OLED-based OCC system schematic diagram. The input data stream in the form of NRZ-OOK is generated in MATLAB and uploaded to the arbitrary waveform generator (AWG–Agilent 33522A, 30 MHz Function/AWG), the output of which is used for intensity modulation of the two OLED (UNISAGA of size 200×50 mm^2 and 0.41 mm thickness) Txs via drivers (Thorlabs LEDD1B). The OLEDs' detailed optical and electrical characteristics in terms of the threshold voltage, bias current, linear dynamic range, optical spectrum, optical radiation patterns and output optical power–current–voltage curves can be found in [1]. Note that using the same OLED Tx, we proposed a LOS OCC link for short- and long-range IoT applications [4]. We achieved a bit error rate below 10^{-6} for indoor short range up to 4 m and 3.56×10^{-3} for outdoor long range up to 120 m links [4].

The experiment setup is depicted in Fig. 2, with the OLEDs and a Raspberry Pi camera (CMOS image sensor) placed facing the wall, see Fig. 2(a), and paper reflectors as in Fig. 2(b). Note that the distance L of 1 m was used to capture the photo of the entire setup; however, for measurement, we used L of 2 m. In this work, we consider two cases of OLED-based Txs being in phase and out of phase. The camera captured the
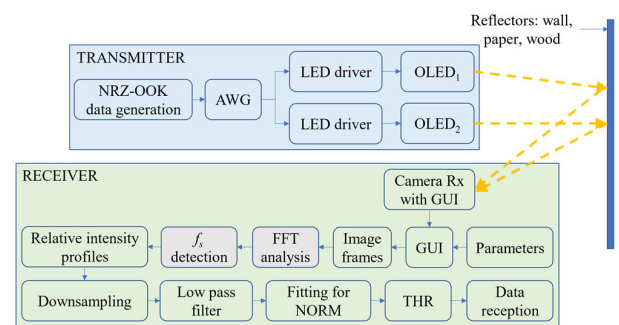

FIGURE 1. Schematic diagram of NLOS MIMO OLED-based OCC.

intensity-modulated light signal reflected from the reflectors (i.e., walls, papers and wooden surfaces) in a dark room setting. For Txs being ON, we measured the illuminance using a lux meter with and without the reflection from the optical table. The measure illuminance values were almost the same at 20 ± 1.4 lx. The Raspberry Pi camera, operating in the RS mode and controlled using a GUI developed in Python, is mounted between the OLEDs to capture the modulated light.

The python-based GUI platform is primarily designed based on four factors [3]: *i*) imports to define the interface
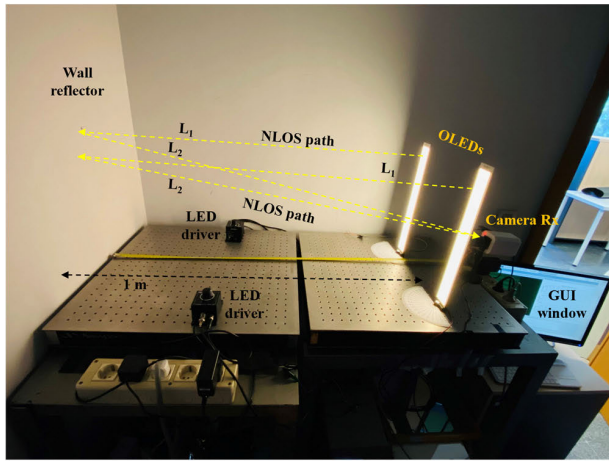
(a)
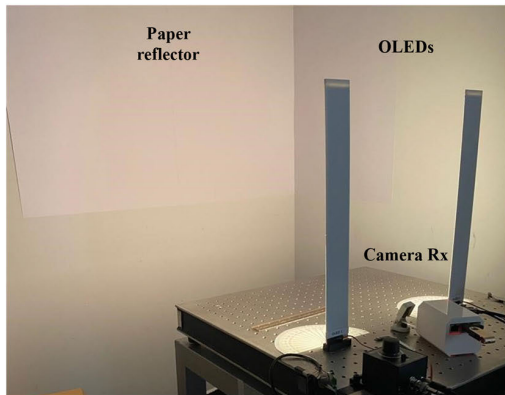
(b)

FIGURE 2. Experimental setup for NLOS MIMO OLED-OCC system with a: (a) wall and (b) paper reflector.

TABLE 2. Key experimental parameters.

Parameter	Description	Value
Two OLED Txs	**Tx₁ and Tx₂**	**UNISAGA**
P	Size	$200 \times 50 \text{ mm}^2$
I_B	Bias current	230 mA
	Device thickness	0.41 mm^2
	Luminous efficiency	53 lm/W
	Luminous flux	75 lm
Camera Rx	**Raspberry Pi**	**V2**
f_c	Focal length	3.04 mm
ρ	Pixel size	1.12 μm
	Resolution	2592×1952 pixels
f_r	Camera frame rate	30 fps
t_{exp}	Exposure time	1000, 1250, 1500 μs
G_v	Camera gain	25, 35, 45 dB
	Camera position	25 cm from base
f_s	Tx frequency	100, 200, 400, and 600 Hz
	N_{bits}; and data throughput with respect to f_s and f_r	100 Hz: 9 bits/frame; 270 bps 200 Hz: 18 bits/frame; 540 bps 400 Hz: 36 bits/frame; 1080 bps 600 Hz: 56 bits/frame; 1680 bps
L	Distance to wall reflector	2 m
P_r	Optical power at Rx	7 lux
ρ_{wall}	Reflectivity of the white wall	0.65 (Blue); 0.75 (Green); and 0.82 (Red)
ρ_{paper}	Reflectivity of the white paper	0.7-0.8 at all visible wavelengths
ρ_{wood}	Reflectivity of the wood	0.5

of different camera modules; *ii*) easy control of camera parameters such as frame rate f_r, t_{exp}, G_v, and the number of frames to be recorded; *iii*) functions for creating and closing sessions for image recording; and *iv*) the window design including title, image preview, and RGB plots, for performing the initial analysis of the received data. As GUI is designed to provide a real-time image preview and RGB plots, it is helpful to perform an initial analysis of the captured data and to adjust camera capturing parameters to improve the quality of the output signal. Note that the GUI allows for the adjustment of the gain of individual R (red), G (green), and B (blue) channels based on the color of the optical source. The RGB gains for the Pi camera V2 were set to default values due to the use of white OLEDs, while the gain of the camera was adjusted to enhance the image quality.

Further offline data processing was performed in MATLAB using traditional image processing techniques. We utilized the GUI-based camera control to set the ROI while recording the data. The GUI session is set to capture 50 data frames at f_r of 30 fps for all values of t_{exp}, f_s, G_v, and L, see Table 2. As for the parameter selection, we refer to

our recently published work on curved OLED-based NLOS SIMO-OCC links [3]. The results in [3] depicted that for a 2 m long NLOS-OCC link with reflections from a wall, the SNR increased by 1 dB and R_{rs} increased by 1% (96–97%) and 4% (83–87%) for f_s of 200 and 600 Hz, respectively with an increase in t_{exp} of 1000–1500 μs and G_v of 25–45 dB. Therefore, we have adopted t_{exp} and G_v in the ranges of 1000 – 1500 μs and 25 – 45 dB, respectively.

The data throughput was calculated based on a number of visible bits/frame, N_{bits} within the ROI with respect to f_s and f_r as bits/frame $\times f_r$. Table 2 also shows the calculated data throughput values.

The FFT on the captured image frames is performed in order to detect f_s for further data processing and analysis. Note that FFT is performed separately for two different use cases, as mentioned before, which will be explained further in section IV. Using the GUI, the combined intensity profiles of RGB channels are captured, then normalized for thresholding and binarization of data frames, and then converted to a vector transformation for decoding the data streams, see Fig. 1. In [3] and [24], authors derived and demonstrated that the intensity profiles can also be used to calculate the SNR considering that the camera has a gain G_v. As a result, G_v can be utilized in highly attenuated situations when the received NLOS signal is weak in order to improve the SNR. Furthermore, the received data bit vector obtained after normalization and thresholding is compared with the transmitted data stream to determine the R_{rs} of the received bits by determining the ratio of the incorrectly decoded bits to the total number of transmitted bits (i.e., the number of bit errors).
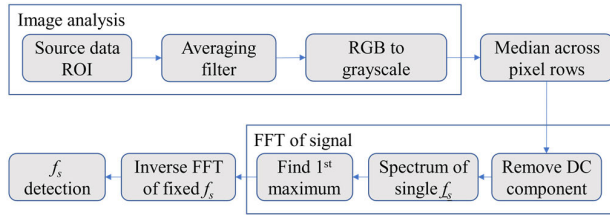
FIGURE 3. The process of FFT for detecting f_s for two in phase OLED Txs.

IV. EXPERIMENT RESULTS AND ANALYSIS

A. IN PHASE OLED TXS

Figure 3 shows the steps involved in the FFT analysis for the detection of modulation frequency f_s when two OLED Txs are in phase, i.e., OLEDs transmitting at the same f_s and are synchronized. Image analysis involves the detection of source data ROI followed by averaging filter $y(n)$ used for smoothing noisy data, which is given:

$$y(n) = \frac{1}{W_s} \text{ones}(1, W_s), \quad (1)$$

where W_s is the ROI window size. Following RGB to grayscale RGB_{gray} conversion, the median across pixel rows operation is carried out, which is given as:

$$\text{Median} = \text{filter}(y(n), 1, \text{RGB}_{\text{gray}}). \quad (2)$$

After removing the DC component from the signal F, to find the signal spectrum and its 1$^{\text{st}}$ maximum spectral line is obtained. Next, IFFT is applied to detect f_s. As outlined previously, we have considered two capturing scenarios of the plain reflector surface and the exact corner of the room with different reflector surfaces.

1) A PLAIN SURFACE

Figure 4 shows examples of captured image frames with their respective intensity profiles, RGB channel histograms, and the spectrum plots for plain reflector surfaces (i.e., wall, paper and wooden door). For the FFT plots we have the following observations:

i) Those plots on the top depict the received signal, similar to the signal plots in one GUI of the captured image. Note that a maximum pixel value of 80 for both wall and paper reflectors, which corresponds to the same reflectivity ρ for wall ρ_{wall} and paper ρ_{paper}, i.e., in the range of 0.7-0.8 for the visible spectrum and assuming Lambertian reflection patterns for plain wall and paper surfaces [25], see Table 2. For the wooden door reflector with ρ_{wood} of 0.5, the maximum pixel value is 50. In addition, the received mean intensity $\bar{I}_r$ profiles i.e., the quantized intensity of the whole image frame within the range of [0-255] were further analyzed as illustrated in Fig. 5. Because of the similar values of ρ, $\bar{I}_r$ for the wall and paper is almost the same for all values of t_{exp} and G_v. Note, $\bar{I}_r$ value increases with an increase in t_{exp} and G_v. $\bar{I}_r$ for wooden door is almost

Algorithm 1 FFT for the detection of f_s for two in-phase OLED Txs

Require: data image frames;
Ensure: f_s detection;
1. Acquire image ROI;
2. Apply averaging filter $y(n)$;
3. Convert to grayscale $y(n)_{\text{img}} \rightarrow \text{RGB}_{\text{gray}}$;
4. Apply median across img pixel lines $\text{RGB}_{\text{gray}} \rightarrow$ *Median*;
5. **for** each RGB_{gray} **do**
6. $\quad yy = \text{median}(\text{RGB}_{\text{gray}})$;
7. $\quad y = \text{filter}(y(n), 1, yy)$;
8. **end for**
9. FFT of signal
10. **for** each y **do**
11. $\quad F = 2*\text{fft}(y).1/(\text{length}(y))$;
12. **end for**
13. Remove DC component $F(1) = 0$; $F(\text{round}(\text{length}(F)/2): \text{end}) = 0$;
14. Spectrum of F: $F_1 = \text{zeros}(\text{length}(F))$;
15. Find the maximum spectral line for f_s detection from F_1;
16. **for** F_1 **do**
17. $\quad [m, i] = \max(\text{abs}(F))$;
18. $\quad F_1(i) = m$;
19. **end for**
20. **Inverse FFT of F_1 to detect f_s: $f_s = \text{ifft}(F_1)$;**

50% lower compared to the reflections from wall and paper. E.g., for t_{exp} of 1500 μs and G_v of 45 dB $\bar{I}_r$ is 40 for both wall and paper reflectors, while it is reduced to 20 for a wooden reflector.

ii) In the plots shown in the center, a red dot indicates the detected spectrum of a fixed single f_s with 1$^{\text{st}}$ maximum spectral line.

iii) The last plot illustrates the IFFT of the single f_s spectral line. Regardless of different values of ρ for different reflective materials, the proposed FFT analysis helps to detect f_s for the plain wall, paper and wooden door reflectors, see Fig. 4.

After performing the FFT for the detection of f_s, further offline data processing is performed in MATLAB using traditional image processing techniques for data recovery, see Fig. 1. Figure 6 illustrates R_{rs} as a function of f_s at L of 2 m and for a range of t_{exp}, and G_v. It can be seen from Fig. 6 that i) R_{rs} decreases with the increasing f_s and increases with t_{exp} and G_v; ii) maximum R_{rs} values of $99 - 100\%$ and $88 - 94\%$ are observed at f_s of 100 and 600 Hz, respectively for both wall and paper reflectors. These values correspond to the same ρ and $\bar{I}_r$ values, see Fig. 5; and iii) for a wooden reflector with ρ_{wood} of 0.5, R_{rs} is reduced to 97–98% and 84–91% at f_s of 100 and 600 Hz, respectively. We will use the results in terms of $\bar{I}_r$ and R_{rs} for the plain surface case as a reference for further analysis in this paper.
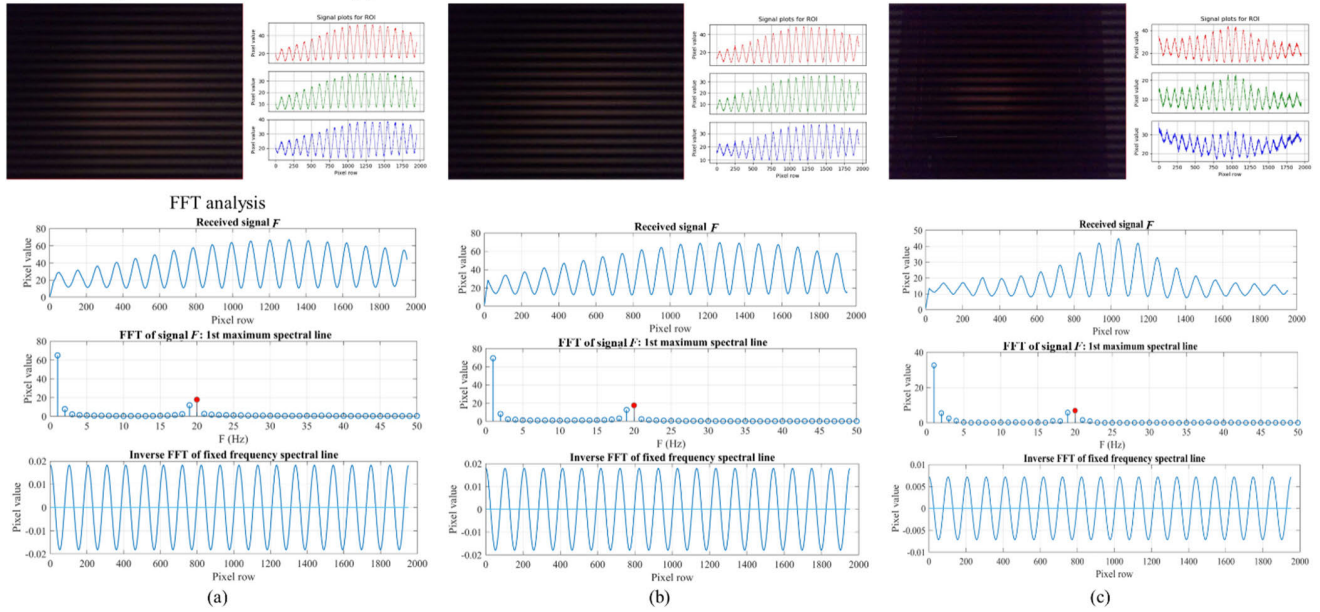
FIGURE 4. Image frames and respective intensity profiles captured and processed using GUI and FFT at $t_{exp} = 1000\mu s$, $G_v = 45$ dB, $L = 2$ m and $f_s = 400$ Hz for (a) wall, (b) paper, and (c) wooden door reflector.
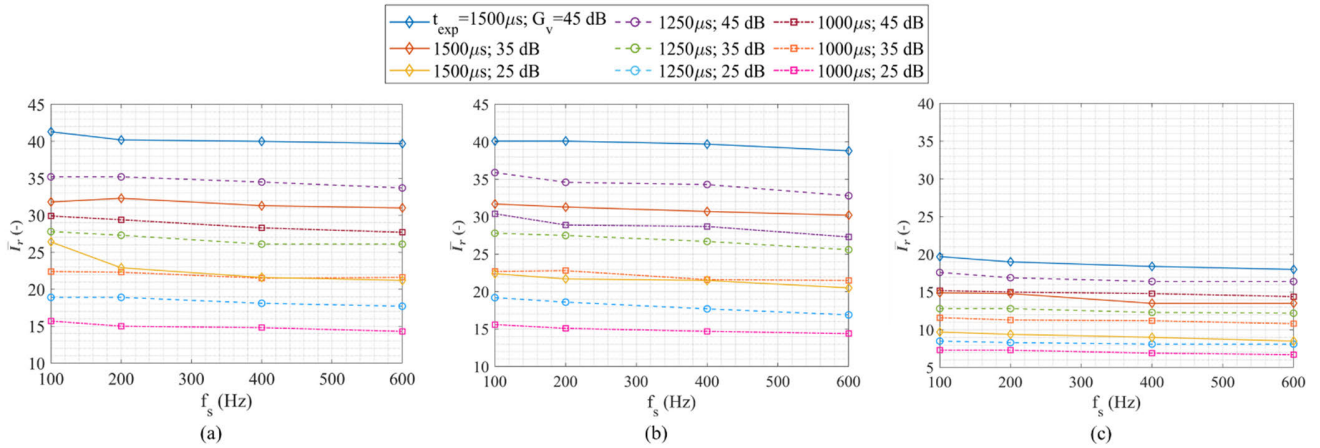

FIGURE 5. Performance analysis in terms of $\bar{I}_r$ vs. fs for the plain surface and a range of t_{exp}, and G_v for: (a) wall, (b) paper, and (c) wooden door reflectors.

2) A ROOM CORNER

Figure 7 shows examples of captured image frames with FFT and IFFT-based generated waveforms and spectrums for the corner of the room with reflections from wall and paper. For the initial analysis, the images were captured only at f_s of 100 and 200 Hz for both wall and paper reflectors. We observe that: *i)* the received signal shows a peak pixel value of ~70 for both reflectors and all f_s; *ii)* the spectrum shows a 1st maximum spectral line at 6 and 10 Hz for the wall and paper reflectors, respectively; and *iii)* the recovered signals.

Figure 8 depicts the distribution of $\bar{I}_r$ at the corner of the room with respect to t_{exp}, G_v, and a range of f_s for both wall and paper reflectors. As previously mentioned in Section III,

$\bar{I}_r$ increases with increasing t_{exp} and G_v. While a very minimal reduction in $\bar{I}_r$ is seen with the increasing f_s. Note, the increase in $\bar{I}_r$ by ~5 (-) compared with Fig. 5 due to the cross reflections from wall and paper surfaces.

Table 3 shows the values of R_{rs} for a range of f_s, G_v and t_{exp} as well as two values of ρ_{wall} and ρ_{paper}. R_{rs} of ~98 and ~95 % are observed at f_s of 100 and 200 Hz, respectively for all values of G_v and t_{exp} and for ρ_{wall} and ρ_{paper}, respectively.

The results in the first two capturing scenarios show the best performance at higher G_v and t_{exp} of 1500 μs and 45 dB, respectively. Therefore, the link performance was tested at t_{exp} of 1500 μs and G_v of 25, 35, and 45 dB for further capturing scenarios.
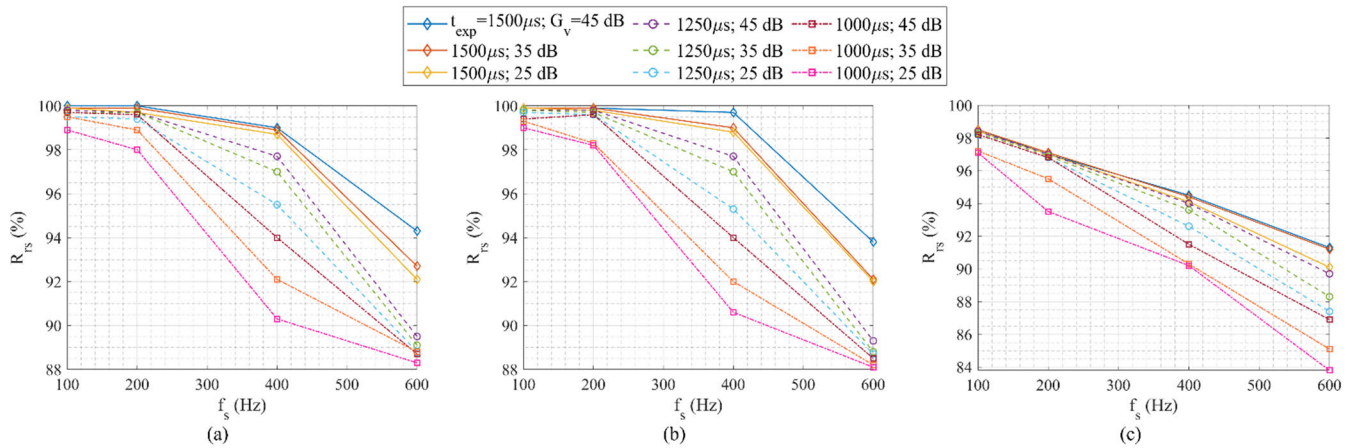
FIGURE 6. R_{rs} versus fs for the plain surface and a range of t_{exp}, and G_v for: (a) wall, (b) paper, and (c) wooden door reflectors.
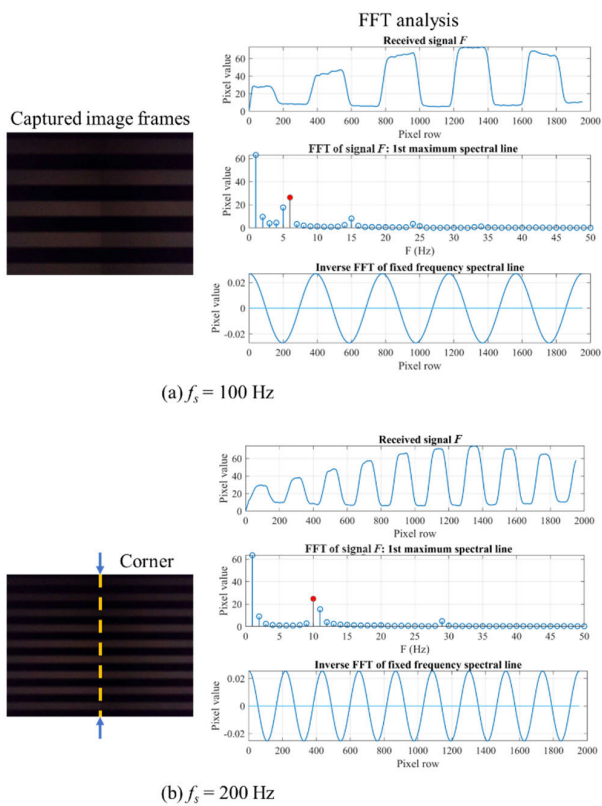

(a) f_s = 100 Hz

(b) f_s = 200 Hz

FIGURE 7. Captured image frames and FFT plots at exact corner at t_{exp} = 1000 μs and G_v = 45 dB for (a) wall, and (b) paper.

B. OUT OF PHASE OLED TXS

Figure 9(a) shows the extended NLOS OLED-based MIMO-OCC system overview for two OLED Txs in different phases. It is expected that when two OLEDs close to each other are transmitting in different phases as well as at different f_s, i.e., f_{s1} and f_{s2} for OLED$_1$ and OLED$_2$, respectively, there will be some interference region on the reflective surface. Therefore, after relative intensity profiles, the images are scanned to detect the maximum power profile, which reflects
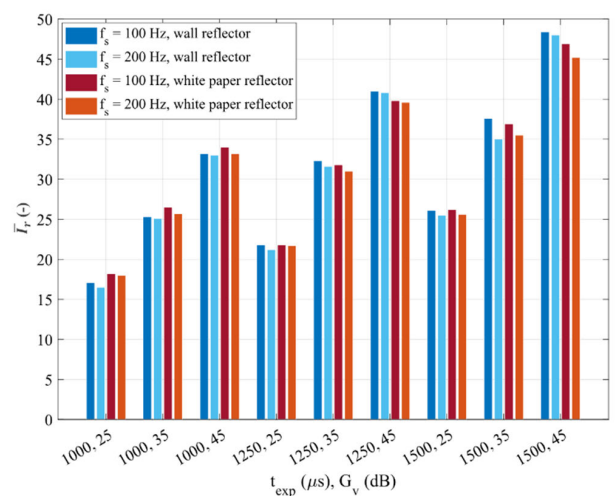

FIGURE 8. Performance analysis in terms of $\bar{I}_r$ at the exact corner of the room with respect to varying f_s, t_{exp}, and G_v for wall and paper reflectors.

TABLE 3. R_{rs} in % at the exact corner of the room for ρ_{wall} and a range of f_s, t_{exp}, and G_v for wall and paper reflectors.

ρ	f_s (Hz)	t_{exp} (μs) / G_v (dB)	1000	1250	1500
ρ_{wall}	100	25	98.2	98.2	98.2
		35	98.2	98.2	98.2
		45	98.6	98.2	98.2
	200	25	96.4	95.3	96.4
		35	95.9	95.9	95.3
		45	95.9	96.4	95.9
ρ_{paper}	100	25	98.8	98.2	98.2
		35	98.2	98.8	98.2
		45	98.2	98.2	98.2
	200	25	95.9	95.9	95.9
		35	95.9	95.9	95.9
		45	95.9	95.9	95.3

the interference region. The detected interference region is then marked as I_{px} and used for further FFT analysis to detect f_{s1} and f_{s2} within I_{px}, see Fig. 9(b). Moreover, the interference analysis and f_s detection play an important role in identifying Txs as OLED$_1$ and OLED$_2$.
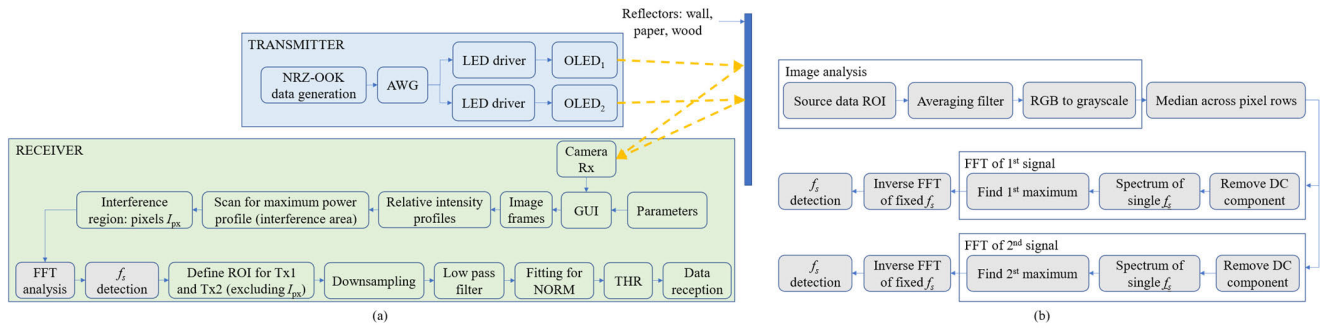
FIGURE 9. NLOS MIMO OLED-based OCC system for: (a) two OLED Txs in different phase, and (b) FFT for f_s detection.

Algorithm 2 FFT analysis for f_s detection: two OLED Txs in different phase

---

Require: data image frames; do the same steps from 1 to 13 as Algorithm 1

Ensure: f_{s1} and f_{s2} detection;
1. Spectrum of F: $F_1 = \text{zeros}(\text{length}(F))$;
    $F_2 = \text{zeros}(\text{length}(F))$;
2. Find maximum spectral line for f_{s1} and f_{s2} detection from F_1 and F_2;
3. **for** F_1 and F_2 **do**
4. $[m, i] = \max(\text{abs}(F))$;
5. $F_1(i) = m$;
6. $F_2(i) = m$;
7. **end for**
8. **Inverse FFT of** F_1 **and** F_2 **to detect** f_s: $f_{s1} = \text{ifft}(F_1)$;
    $f_{s2} = \text{ifft}(F_2)$;

For the FFT of two OLED Txs in different phases, the same steps as steps 1 to 13 are followed from Algorithm 1. After determining the median and removing the DC component offset, the maximum spectral line, i.e., the 1st and 2nd maximum for f_{s1} and f_{s2}, respectively, is determined. The IFFT is applied over the spectrum of F, F_1, and F_2 to detect the f_{s1} and f_{s2}. Two different scenarios such as two OLED Txs transmitting at the same f_s in different phases and at different f_s capturing at plain reflector surface, are considered.

1) OLED TXS TRANSMITTING AT SAME F_S
Figure 10 shows examples of captured image frames with the FFT plots when two OLED Txs are transmitting at the same f_s in different phases captured at the plain reflector surface of the room for wall and paper reflectors. It can be seen from captured image frames in Fig. 10, that *i)* the I_{px} and OLED$_1$ and OLED$_2$ regions are well detected by scanning for maximum power profile as shown in Fig. 9(b); and *ii)* the received signal intensity profiles are affected due to I_{px} and, therefore, not much pixel value difference is seen between 1 and 0 bit, see received signal plots in Fig. 10. However, based on the proposed FFT, it can be seen that the spectrums of f_{s1} and f_{s2} are well detected and hence the perfect f_s detection for both OLEDs at wall as well as paper reflectors.

FIGURE 10. Captured image frames and FFT plots at $f_s = 100$ Hz, $t_{exp} = 1500 \mu s$ and $G_v = 25$ dB for (a) wall, and (b) paper.

TABLE 4. Performance analysis in terms of R_{rs} in % at t_{exp} of 1500 μs with respect to varying f_s and G_v for wall, and paper reflectors.

ρ	G_v (dB)	25	35	45
	f_s (Hz)			
ρ_{wall}	100	100	100	100
	200	99	100	100
	400	98	98	98
	600	92	93	94
ρ_{paper}	100	100	100	100
	200	99	99	100
	400	98	99	99
	600	92	92	94

After the f_s detection, the performance in this scenario was analyzed further for R_{rs}. Table 4 shows R_{rs} values for t_{exp} of

FFT analysis

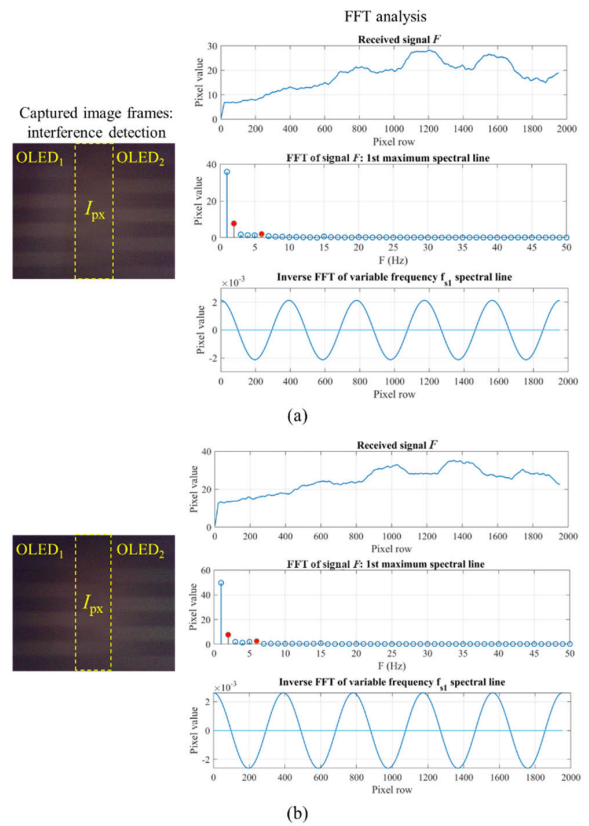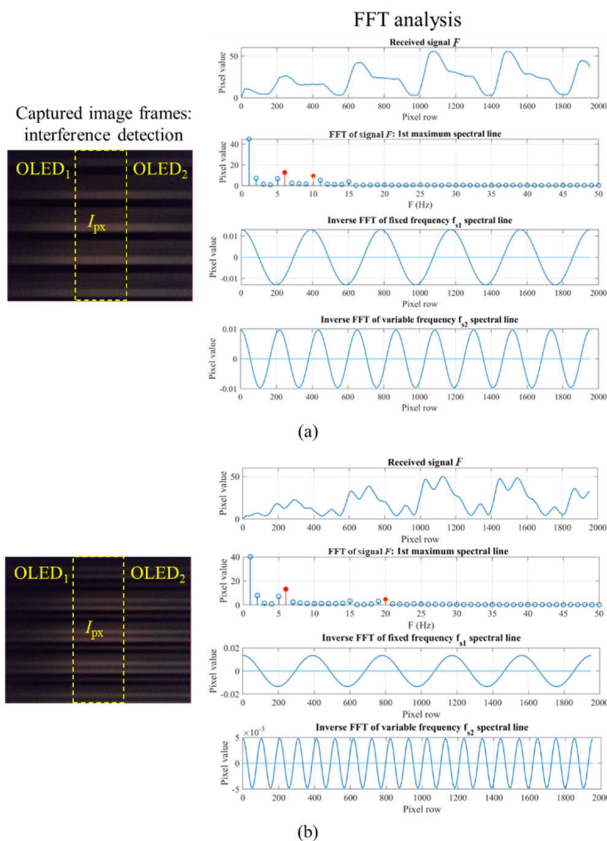**FIGURE 11.** Captured image frames and FFT plots at $f_s = 100$ Hz, $t_{exp} = 1500 \mu$s and $G_v = 25$ dB for (a) wall, and (b) paper.

1500 μs for a range of f_s and G_v for wall, and paper reflectors. It can be seen that, regardless of the I_{px} region and due to the accurate detection of OLED$_1$ and OLED$_2$ regions using the scanning function, Fig. 9(a), R_{rs} of 100 % was achieved at f_s of 100 and 200 Hz for wall and paper reflector and at G_v of 45 dB. Therefore, even with the I_{px} region, the performance in this case is similar to that in Section IV-A.

2) OLED TXS TRANSMITTING AT DIFFERENT F_S

Figure 11 shows the examples of captured image frames with the FFT plots captured when two OLED Txs are transmitting at different f_s, i.e., f_{s1} and f_{s2} for OLED$_1$ and OLED$_2$, respectively at the plain wall and paper reflectors.

It can be seen from captured image frames in Fig. 11, that i) the I_{px} region is widened due to the mixing of two different f_s; ii) the received signal intensity profiles are affected due to the widened I_{px} as compared to the previous scenario of same f_s in different phase and therefore not much pixel value difference is seen between 1 and 0 bit, see received signal plots in Fig. 11 and iii) the received intensity profiles looks similar to a 4-PAM signal due to mixing of two different f_s, for example f_{s1} of 100 Hz and f_{s2} of 400 Hz, see Fig. 11(b). Note, in this case f_{s1} was fixed to 100 Hz and f_{s2} was varied at values of 200 and 400 Hz. Regardless of distorted intensity profiles, it can be seen that the spectrums of f_{s1} and f_{s2} are well

TABLE 5. Performance analysis in terms of R_{rs} in % at t_{exp} of 1500 μs with respect to varying f_s and G_v for wall, and paper reflectors.

ρ	f_s (Hz)	G_v (dB) 25	35	45
ρ_{wall}	$f_{s1} = 100$	96	98	98
	$f_{s2} = 200$	94	96	96
	$f_{s1} = 100$	95	95	95
	$f_{s2} = 400$	88	89	89
ρ_{paper}	$f_{s1} = 100$	96	97	98
	$f_{s2} = 200$	94	95	96
	$f_{s1} = 100$	95	95	96
	$f_{s1} = 400$	88	88	90

detected and hence the perfect f_s detection for both OLEDs at wall as well as paper reflectors.

Table 5 shows R_{rs} values at t_{exp} of 1500 μs for a range of f_{s1} and f_{s2} and G_v values for wall, and paper reflectors. It can be seen that for wall and paper reflector at G_v of 45 dB; i) R_{rs} of 98 and 96 % was achieved at f_{s1} of 100 and f_{s2} of 200 Hz, respectively; and ii) R_{rs} of 95-96 and 89-90 % was achieved at f_{s1} of 100 and f_{s2} of 400 Hz, respectively.

C. LATENCY OF THE PROPOSED SCHEME

The latency in OCC depends mainly on the image acquisition and processing. The hardware involved in acquisition is the image sensor for capturing with time t_{cap}, which transfers raw image data to the computer's CPU at time t_{trans} using a camera serial interface (CSI). In the case of the Raspberry Pi, the CPU has a dedicated image signal processor (ISP) that performs the JPEG or H.264 encoding with time t_{encode}. Finally, the OCC image processing happens in the CPU using MATLAB in time t_{proc}. Therefore, the overall latency can be calculated by adding together the image acquisition and processing times as:

$$Latency = t_{cap} + t_{trans} + t_{encode} + t_{proc}. \tag{3}$$

We now define every term separately to calculate the time required in every step as:

Image sensor capturing, t_{cap}: induces a delay that depends on the rolling shutter sampling process, that can be estimated as:

$$t_{cap} = t_{rs} \times N_{bits} + t_{exp} + t_{readout} + t_{reset}, \tag{4}$$

where t_{rs} is row sampling time which is 18.904 μs for Raspberry Pi camera module [26], $t_{readout}$ is readout time and t_{reset} is row rest time. Note, $t_{readout}$ and t_{reset} are negligible values (very small value). For example, at f_s of 100 Hz, 9 bits are visible in one frame and t_{exp} of 1000 μs, t_{cap} is 1170.136 μs (0.001170136 s).

For different hardware dependent parts, we can then enumerate following:

- CSI, t_{trans}: the serial bus takes raw frames that weight 24.2 MB each and has a data transfer rate of 2.9 Gbps to the ISP, adding a delay in terms of t_{trans} which is 0.0667 s for raspberry pi camera module V2 [26].
- ISP, t_{encode}: the ISP applies demosaicing, white balance, noise reduction, and other processes to the raw image

TABLE 6. Summary of results in terms of R_{rs} in %.

Capturing scenario	f_s (Hz)	f_s detection using FFT	ρ_{wall}	ρ_{paper}	ρ_{wood}
Two OLED Txs in phase					
Plain surface	100	✓	100	100	98
	200	✓	100	100	97
	400	✓	99	99	95
	600	✓	94	94	92
Exact corner	100	✓	98	98	-
	200	✓	96	95	-
Two OLED Txs in different phases					
Transmitting at same f_s	100	✓	100	100	-
	200	✓	100	100	-
	400	✓	98	99	-
	600	✓	94	94	-
f_{s1} = 100 Hz; f_{s2} = 200 Hz	100	✓	98	98	-
	200	✓	96	96	-
f_{s1} = 100 Hz; f_{s2} = 400 Hz	100	✓	95	96	-
	400	✓	89	90	-

data, and converts it into JPEG/H.264 format. Typical ISP processing rates can range from 100 to 400 Mpx/s. For example, the delay added by the ISP as t_{encode} can be estimated as 8Mpx/(100 Mpx/s) = 0.08 s [26].

- MATLAB Image Processing for FFT analysis, t_{proc}: Although the offline processing is not directly comparable to a real online processing, we estimated our scrip to take t_{proc} of 0.7 s/frame for all values of f_s in case of in phase OLED Txs transmitting at same f_s and 1.2 s/frame in case of interference analysis for out of phase OLED Txs with same and different f_s.

Therefore, the overall latency within the proposed NLOS MIMO OLED-based OCC at f_s of 100 Hz and t_{exp} of 1000 μs can be estimated using Eq. (3) and (4), for all values of f_s in case of in phase OLED Txs transmitting at same f_s is 0.84787 s (t_{cap} (0.001170136 s) + t_{trans} (0.0667 s) + t_{encode} (0.08 s) + t_{proc} (0.7)) and in case of interference analysis for out of phase OLED Txs with same and different f_s is 1.34787 s.

V. SUMMARY
The performance of the proposed NLOS OLED based MIMO-OCC scheme is summarized in Table 6.

It can be seen that:

For two OLED Txs in phase:

i) R_{rs} of 100 % was achieved at f_s of 100 and 200 Hz while the R_{rs} was reduced to 99 and 94 % for f_s of 400 and 600 Hz, respectively for plain wall and paper reflectors. While at plain wooden surface with reduced ρ_{wood} of 0.5, R_{rs} is reduced to 98 and 92 % at f_s of 100 and 600 Hz, respectively and

ii) at the exact corner of the room with wall and paper reflectors, R_{rs} of 98 and 96 % were achieved at f_s of 100 and 200 Hz, respectively.

For two OLED Txs out of phase for wall and paper reflector:

i) when both OLEDs are transmitting at f_{s1} of 100 Hz and f_{s2} of 200 Hz, R_{rs} of 98 and 96 %, respectively was achieved and

ii) when both OLEDs are transmitting at f_{s1} of 100 Hz and f_{s2} of 400 Hz, R_{rs} of 95-96 and 89-90 %, respectively was achieved.

Note, in all the above cases, accurate, i.e., 100 % fs detection was performed using the proposed FFT that helps to determine the Tx as well as its respective f_s value when transmitting in NLOS MIMO scenarios.

Based on the summary of results, we showed that FFT performs accurate f_s detection along with acceptable data reception values of above ∼90 % in all the proposed scenarios. This solution helps to analyze various interference scenarios in terms of f_s for multiple Txs in an indoor environment as described in this paper along with NLOS MIMO-OCC link performance.

VI. CONCLUSION AND FUTURE SCOPE
In this paper, for the first time, to the best of our knowledge, we proposed NLOS OLED-based MIMO-OCC link and carried out a performance analysis and evaluation for various indoor scenarios. We carried out an experimental investigation of the proposed NLOS MIMO-OCC link using two OLEDs and a camera as Txs and the Rx, respectively, as well as reflections from various different surfaces such as plain wall, paper and wooden surfaces as well as from the corner of the room. Two different scenarios with two OLED Txs that are i) in phase (i.e., synchronized) and transmitting at the same frequency f_s; and ii) out of phase and with different f_s at different reflective and surface materials. Moreover, we carried out FFT for f_s detection and interference analysis when both the OLEDs are transmitting in different phase as well as at different f_s. The results depicted that, at higher t_{exp} of 1500, G_v of 45 dB and a link span of 2 m an acceptable performance in terms of R_{rs} of 90-100 % was achieved in all the scenarios with 100 % f_s detection using proposed FFT.

As a part of future works, the proposed scheme can be tested by adding more than two OLEDs with different sizes and shapes considering more diverse and dynamic indoor environments and reflective materials and with complex simulation-based analyses of different indoor scenarios to validate the robustness of the proposed scheme under various real-world conditions. The computational complexity of the proposed FFT-based frequency detection scheme can be further investigated by increasing the signal length using complex modulation formats and adding more OLEDs to support applications such as indoor localizations and device-to-device communication in smart indoor environments. Moreover, future work could include investigation of MIMO-NLOS OCC systems using (i) OLEDs of different size and shapes in public places such as airports, shopping centers, train, and bus stations; and (ii) flexible or flat panel display technology in wearable biomedical devices in hospitals for information display, data communications and indoor

localization can be further investigated. Moreover, as suggested in [21], [22], and [23] the data rate of the proposed NLOS MIMO-OCC scheme can be improved by adopting the different modulation formats such as multi-level PAM, PSK, PWM and OFDM. Note that, the latency can be improved with implementing real-time system in future by developing mobile app or real time desktop app by further extending the proposed GUI platform for data processing and giving final results. For example, the latency can be reduced to 5.883 and 5.346 ms using iPhone 8 Plus and Samsung S8, respectively when processing 10 rows within the image frame at f_r of 30 fps [27].

REFERENCES

[1] Z. N. Chaleshtori, A. Burton, S. Zvanovec, Z. Ghassemlooy, and P. Chvojka, "Comprehensive optical and electrical characterization and evaluation of organic light-emitting diodes for visible light communication," *Opt. Eng.*, vol. 59, no. 4, Apr. 2020, Art. no. 046106.

[2] H. Chun, C.-J. Chiang, and D. C. O'Brien, "Visible light communication using OLEDs: Illumination and channel modeling," in *Proc. Int. Workshop Opt. Wireless Commun. (IWOW)*, Pisa, Italy, Oct. 2012, pp. 1–3.

[3] S. R. Teli, V. Matus, C. L. Aguiar, R. Perez-Jimenez, Z. Ghassemlooy, and S. Zvanovec, "Curved OLED-based NLOS optical camera communications links," *Appl. Opt.*, vol. 62, no. 30, p. 8204, 2023.

[4] P. Chavez-Burbano, S. Vitek, S. R. Teli, V. Guerra, J. Rabadan, R. Perez-Jimenez, and S. Zvanovec, "Optical camera communication system for Internet of Things based on organic light emitting diodes," *Electron. Lett.*, vol. 55, no. 6, pp. 334–336, Mar. 2019.

[5] C.-W. Chow, Y. Liu, C.-H. Yeh, Y.-H. Chang, Y.-S. Lin, K.-L. Hsu, X.-L. Liao, and K.-H. Lin, "Display light panel and rolling shutter image sensor based optical camera communication (OCC) using frame-averaging background removal and neural network," *J. Lightw. Technol.*, vol. 39, no. 13, pp. 4360–4366, Jul. 1, 2021.

[6] P. Luo, M. Zhang, Z. Ghassemlooy, H. Le Minh, H.-M. Tsai, X. Tang, and D. Han, "Experimental demonstration of a 1024-QAM optical camera communication system," *IEEE Photon. Technol. Lett.*, vol. 28, no. 2, pp. 139–142, Jan. 15, 2016.

[7] P. Huynh, T.-H. Do, and M. Yoo, "A probability-based algorithm using image sensors to track the LED in a vehicle visible light communication system," *Sensors*, vol. 17, no. 2, p. 347, Feb. 2017.

[8] W. Wang, C. Chow, L. Wei, Y. Liu, and C. Yeh, "Long distance non—Line-of-sight (NLOS) visible light signal detection based on rolling-shutter-patterning of mobile-phone camera," *Optics Exp.*, vol. 9, no. 25, pp. 10103–10108, 2017.

[9] O. S. Sitanggang, V. L. Nguyen, H. Nguyen, R. F. Pamungkas, M. M. Faridh, and Y. M. Jang, "Design and implementation of a 2D MIMO OCC system based on deep learning," *Sensors*, vol. 23, no. 17, p. 7637, Sep. 2023.

[10] W. J. Ryu and S. Y. Shin, "RGB MIMO optical camera communication with Histogram equalization," in *Proc. Int. Conf. Signals Syst. (ICSigSys)*, Bali, Indonesia, 2017, pp. 303–307.

[11] C. Jurado-Verdu, V. Guerra, V. Matus, J. Rabadan, and R. Perez-Jimenez, "Convolutional autoencoder for exposure effects equalization and noise mitigation in optical camera communication," *Opt. Exp.*, vol. 29, no. 15, p. 22973, 2021.

[12] P. Luo, M. Zhang, Z. Ghassemlooy, S. Zvanovec, S. Feng, and P. Zhang, "Undersampled-based modulation schemes for optical camera communications," *IEEE Commun. Mag.*, vol. 56, no. 2, pp. 204–212, Feb. 2018.

[13] H. Farahneh, C. Mekhiel, A. Khalifeh, W. Farjow, and X. Fernando, "Shadowing effects on visible light communication channels," in *Proc. IEEE Can. Conf. Electr. Comput. Eng. (CCECE)*, Farah, BC, Canada, May 2016, pp. 1–5.

[14] S.-Q. Chen, X.-F. Chi, and T.-Y. Li, "Non-line-of-sight optical camera communication aided by a pilot," *Opt. Lett.*, vol. 46, no. 14, pp. 3348–3351, 2021.

[15] Z. Zhang, T. Zhang, J. Zhou, Y. Lu, and Y. Qiao, "Mobile phone camera based visible light communication using non-line-of-sight (NLOS) link," in *Proc. Int. Conf. Netw. Infrastruct. Digit. Content (IC-NIDC)*, Guizhou, China, Aug. 2018, pp. 35–39.

[16] W. Hong, T. Li, W. Li, and X. Shi, "Analysis of DCO-OFDM for indoor visible light communications," *J. Phys., Conf. Ser.*, vol. 1606, no. 1, Aug. 2020, Art. no. 012005.

[17] X. Liu, J. Li, J. Li, and Z. Huang, "Analysis of the single-FFT receiver for layered ACO-OFDM in visible light communications," *J. Lightw. Technol.*, vol. 38, no. 17, pp. 4757–4764, Sep. 1, 2020.

[18] B. Wang, W. Sun, J. Chen, and C. Yu, "Frequency domain anti-flickering in visible light communication system," *Opt. Commun.*, vol. 516, Aug. 2022, Art. no. 128203.

[19] N. Bani Hassan, Z. Ghassemlooy, S. Zvanovec, M. Biagi, A. M. Vegni, M. Zhang, and P. Luo, "Non-line-of-sight MIMO space-time division multiplexing visible light optical camera communications," *J. Lightw. Technol.*, vol. 37, no. 10, pp. 2409–2417, May 15, 2019.

[20] W.-C. Wang, C.-W. Chow, L.-Y. Wei, Y. Liu, and C.-H. Yeh, "Long distance non-line-of-sight (NLOS) visible light signal detection based on rolling-shutter-patterning of mobile-phone camera," *Opt. Exp.*, vol. 25, no. 9, p. 10103, 2017.

[21] Z. Liu, L. Yang, Y. Yang, R. Wu, L. Zhang, L. Chen, D. Wu, and J. She, "Improved optical camera communication systems using a freeform lens," *Opt. Exp.*, vol. 29, no. 21, p. 34066, 2021.

[22] N. Jiang, B. Lin, Q. Lai, T. Huang, Z. Ghassemlooy, O. I. Younus, J. Luo, Y. Xie, L. Dai, and Z. Huang, "Non-line-of-sight WDM-MIMO optical camera communications with the DBPWR algorithm," *Opt. Commun.*, vol. 518, Sep. 2022, Art. no. 128371.

[23] F. Yang, S. Li, Z. Yang, C. Qian, and T. Gu, "Spatial multiplexing for non-line-of-sight light-to-camera communications," *IEEE Trans. Mobile Comput.*, vol. 18, no. 11, pp. 2660–2671, Nov. 2019.

[24] V. Matus, V. Guerra, S. Zvanovec, J. Rabadan, and R. Perez-Jimenez, "Sandstorm effect on experimental optical camera communication," *Appl. Opt.*, vol. 60, no. 1, p. 75, 2021.

[25] K. Lee, H. Park, and J. R. Barry, "Indoor channel characteristics for visible light communications," *IEEE Commun. Lett.*, vol. 15, no. 2, pp. 217–219, Feb. 2011.

[26] Raspberry Pi Datasheets. *Raspberry Pi Image Signal Processor (PiSP) Specification*. Accessed: Apr. 1, 2024. [Online]. Available: chrome-extension://efaidnbmnnnibpcajpcglclefindmkaj/https://datasheets.raspberrypi.com/camera/raspberry-pi-image-signal-processor-specification.pdf

[27] P. Zhang, Q. Wang, Y. Yang, Y. Wang, Y. Sun, W. Xu, J. Luo, and L. Chen, "Enhancing the performance of optical camera communication via accumulative sampling," *Opt. Exp.*, vol. 29, no. 12, p. 19015, 2021.

SHIVANI RAJENDRA TELI received the bachelor's degree from Savitribai Phule Pune University, Maharashtra, India, in 2015, the M.Sc. degree from the Department of Information and Communications Engineering, Pukyong National University, Busan, South Korea, in 2018, and the Ph.D. degree from the Faculty of Electrical Engineering, Czech Technical University (CTU) in Prague, in 2021, within "Visible light-based interoperability and networking (ViSIoN)," which is a project under European Union's Horizon H2020 Marie Skłodowska-Curie Innovative Training Network (MSCA ITN). She is currently a Postdoctoral Researcher with the CTU Global Fellowship Program. Her research interests include wireless communication systems, visible light communications, and optical camera communications for the Internet of Things and sensor networks.

VICENTE MATUS ICAZA received the degree in electrical engineering from the University of Chile, in 2018, and the Ph.D. degree from the University of Las Palmas de Gran Canaria (ULPGC), Spain, in 2021. He was a Marie S. Curie Fellow with the Horizon 2020 Program of European Union for the ITN-VISION Project. He is currently a Researcher with the Photonics Division, Institute for Technological Development and Innovation in Communications (IDeTIC), ULPGC, and a Visiting Researcher with the Instituto de Telecomunicações Aveiro, Portugal, funded by the Catalina Ruiz 2022 Scholarship from the Canary Islands Government. His research interests include the experimental development and deployment of optical wireless communication systems, specifically those based on using cameras as receivers (optical camera communication) and their outdoor applications for wireless sensor networks, the automation of agriculture systems, vehicular communication, and wearable sensors for medical applications.

STANISLAV VÍTEK received the M.Sc. and Ph.D. degrees from the Faculty of Electrical Engineering, Czech Technical University (CTU) in Prague, Prague, Czech Republic, in 2002 and 2008, respectively. He is currently an Assistant Professor with the Department of Radioelectronics, Faculty of Electrical Engineering, CTU. He is a member of numerous international teams focused to networks of robotic telescopes. His main research interests include signal and image processing, embedded systems, machine learning, and database systems.

RAFAEL PEREZ-JIMENEZ was born in Madrid, in 1965. He received the M.S. degree from the Universidad Politécnica de Madrid, Spain, in 1991, the Ph.D. degree (Hons.) from the Universidad de Las Palmas de Gran Canaria (ULPGC), Spain, in 1995, and the Ph.D. degree in history from the Universidad de La Laguna, in 2020. He is currently a Full Professor with ULPGC, where he works in the IDeTIC Research Institute. His current research interests include optical camera communications (OCC), optical indoor channel characterization, and the design of robust visible light communications (VLC) systems for indoor communications, especially applied for joint communications and sensing. He received the Gran Canaria Science Prize, in 2007, the Vodaphone Foundation Research Award, in 2010, and the RSEAPGC Honor Medal, in 2017.

ZABIH GHASSEMLOOY (Senior Member, IEEE) received the B.Sc. degree (Hons.) from Manchester Metropolitan University, U.K., in 1981, and the M.Sc. and Ph.D. degrees from Manchester University, U.K., in 1984 and 1987, respectively. From 1987 to 1988, he was a Postdoctoral Research Fellow with City University, U.K. From 1988 to 2004, he was with Sheffield Hallam University, U.K. From 2004 to 2014, he was the Associate Dean of Research with the Faculty of Engineering and Environment, Northumbria University, U.K. He is currently the Head of the Photonics Technology Laboratory and Optical Communications Research Group. He was a Research Fellow (2016–2022) and a Distinguished Professor (2015–2022) with Chinese Academy of Science. He was a visiting professor several universities. He was the Vice-Chair of EU Cost-Action IC1101 (2011–2016) and is the Vice-Chair of Cost Action CA19111 (2020–2024). He was an IEEE Distinguished Lecturer (2024–2025). He has been the Founder of European Collaborative Research Network, since 2020. His research interests include optical wireless communications (OWC), free space optics, visible light communications, optical camera communications, and hybrid RF-OWC, with many funded research projects from Research Council (U.K.), U.K. Space Agency, European Union, and industries in collaboration with international research centres. Over 990 publications (429 journals and eight books), over 115 keynote/invited talks, supervised 12 research fellows, and 75 Ph.D.'s. He was a Chief Editor of *British Journal of Applied Science & Technology* and *International Journal of Optics and Applications*, an associate editor of several journals (IEEE and IET), and a co-guest editor of many special issues on OWC. He has been the Vice-Chair of OSA Technical Group of Optics in Digital Systems, since 2018, the Chair of IEEE Student-Branch from Northumbria University, since 2019. From 2004 to 2006, he was the IEEE U.K./IR Communications Chapter Secretary, the Vice-Chair (2006–2008), the Chair (2008–2011), and the Chair of IET Northumbria Network (2011–2015). He is also the Founder and the Chair of the IEEE/IET International Symposium on Communications Systems, Networks and DSP, West Asian Symposium on Optical and mmW Wireless Communications, and South American Colloquium on Visible Light Communications; and the Co-Founder of several international events, including Workshop on Optical Wireless Communications in IEEE ICC, since 2015, Colloquium on OWC in CSNDSP, since 2004, and International Workshop on OWC, since 2015. He is a fellow of OPTICA and IET; a member of IAENG, and C.Eng.; and Google Scholar Citation: 22570, Google Scholar H-index: 63, and i10-index: 426. He is a member of international technical committee of a very large number of international conferences. He has been the Vice-Chair of OSA Technical Group of Optics in Digital Systems, since 2018.

STANISLAV ZVANOVEC (Senior Member, IEEE) received the M.Sc. and Ph.D. degrees from the Faculty of Electrical Engineering, Czech Technical University (CTU) in Prague, in 2002 and 2006, respectively. He is currently a Full Professor and the Deputy Head of the Department of Electromagnetic Field and the Chairperson of the Ph.D. Branch, CTU. He is the author of two books (and the co-author of the recent book *Visible Light Communications: Theory and Applications*), several book chapters, and more than 300 journals and conference papers. His current research interests include free space optical and fiber optical systems, visible light communications, OLED, RF over optics, and electromagnetic wave propagation issues for millimeter wave bands.

• • •